

An Ultradeep High Resolution X-ray Image of M101:

The X-ray Source Population in a Late-type Spiral

Q. Daniel Wang

Dearborn Observatory, Northwestern University
2131 Sheridan Road, Evanston, IL 60208-2900
Electronic mail: wqd@nwu.edu

Stefan Immler & Wolfgang Pietsch

Max-Planck-Institut für extraterrestrische Physik
Postfach 1603, D-85740 Garching, Germany
Electronic mail: simmler@mpe.mpg.de & wnp@mpe.mpg.de

ABSTRACT

We have studied the X-ray source population of the face-on spiral galaxy M101 (NGC 5457). Within a field of radius $17'$ (36 kpc at the distance of 7.2 Mpc), covered by an ultradeep (229 ks) *ROSAT* HRI image, 51 X-ray sources are detected with signal-to-noise ratios greater than 3.5. About half of these sources are associated with the galaxy. The luminosity of these galactic sources individually ranges from $\sim 4 \times 10^{37}$ to 2×10^{39} ergs s $^{-1}$ in the 0.5-2 keV band. The average luminosity distribution of the sources can be characterized by a power law function: $dN/dL_x = 9.5 L_x^{-1.9}$ sources per 10^{38} ergs s $^{-1}$.

Combined with archival data from the *ROSAT* PSPC, the *Einstein* IPC, and the *ASCA* GIS, we have examined spatial, spectral, and timing properties of the X-ray sources. In particular, we have explored the nature of various superluminous X-ray sources with luminosities significantly greater than the Eddington limit ($\sim 2 \times 10^{38}$ ergs s $^{-1}$) for a $\sim 1.6 M_\odot$ object (neutron star). These X-ray sources, detected in various *ROSAT* HRI and PSPC observations, are not transients and appear to result from recent massive star formation in outer spiral arms. 3 superluminous PSPC sources are associated with giant HII complexes and are clearly resolved. 2 other superluminous RHRI sources are likely associated with shell-like supernova (or more likely hypernova) remnants, which are known to be abnormally luminous in optical and/or radio. We further identify 2 superluminous sources, which all show highly-absorbed X-ray spectra and time variability during and/or between the observations, as candidates for X-ray binary systems that contain black holes.

A comparison of 7 nearby spirals shows that their X-ray source luminosity distributions, normalized by total H I masses, are very similar. But both the number of superluminous X-ray sources and the total X-ray luminosity appear to be correlated with the star forming rate of a galaxy.

Subject headings: galaxies: general — galaxies: spiral — galaxies: ISM — galaxies: starburst — ISM: HII regions — X-ray: general — X-ray: ISM

1. Introduction

Soft X-ray investigation of nearby galaxies is essential for our understanding of high energy phenomena and their relations to galaxy evolution. Such a study avoids much of the usual difficulty in determining the distances to X-ray sources in our own Galaxy. For face-on galaxies at high Galactic latitudes, line-of-sight soft X-ray absorption is minimal, which can be particularly important for observing sources with soft X-ray spectra, such as supernova remnants (SNRs) and superbubbles. These galaxies also allow for rigorous cross-examinations of various galactic components and their interplay. Of course, the understanding of X-ray source populations in nearby galaxies is critical for correctly interpreting X-ray observations of distant galaxies.

As a nearly face-on, grand-design spiral in a direction of exceptionally low foreground Galactic extinction (Table 1; Fig. 1), M101 is a prime target for characterizing the overall properties of galactic X-ray sources. X-ray emission from this galaxy was first observed with the Imaging Proportional Counter (IPC) on board the *Einstein* X-ray Observatory (McCammon & Sanders 1984; Trinchieri, Fabbiano, & Romaine 1990, TFR hereafter). The IPC observations show an apparent over-density of bright X-ray sources in the field of M101. The luminosity of these sources, if located at the distance of the galaxy, is individually a few times $10^{38} - 10^{39}$ ergs s⁻¹ in the IPC 0.16-3.5 keV band, significantly greater than the Eddington luminosity $\sim 2 \times 10^{38}$ ergs s⁻¹ for a $\sim 1.6M_{\odot}$ object (e.g., neutron star). The presence of such superluminous sources (SLS) is also evident in the fields of several other nearby galaxies (e.g., Long & Van Speybroeck 1983). Naturally, these sources have been suggested as X-ray binary systems containing stellar mass black hole candidates (BHCs). With the limited sensitivity and spatial resolution of the IPC observations, however, one cannot rule out the possibility that some of the SLS are actually composites of multiple X-ray-emitting objects (e.g., Fabbiano 1998).

Relatively recent observations from *ROSAT* have provided new opportunities to study X-ray sources in M101. Based on a 34.5 ks exposure with the PSPC (Position Sensitive Proportional Counter; Pfeffermann et al. 1987), Snowden & Pietsch (1995) have shown that a substantial fraction of the observed X-ray emission, primarily at $\sim 1/4$ keV, is unresolved, indicating the presence of the hot interstellar medium (ISM) in the galaxy. Using the same PSPC observation and a short 18.4 ks *ROSAT* HRI (High Resolution Imager — RHRI; David et al. 1996), Williams & Chu (1995) have further suggested that giant HII complexes (GHCs) are responsible for several of the discrete X-ray sources detected in the field of the galaxy. These GHCs are recent starburst regions brighter in both optical and radio than the LMC 30 Dor complex, which contains various luminous X-ray sources: the stellar mass BHC LMC X-1, 30 Dor nebula, LMC-2 superbubble,

and several young SNRs (Wang & Helfand 1991). These studies have demonstrated that M101 is an ideal site to examine the galactic-wide X-ray source population, not only under normal circumstances but also under various starburst conditions.

We have obtained new deep exposures of M101 with the *ROSAT* HRI. Together with existing observations, we constructed an RHRI image with a total exposure time of 229 ks. This single ultradeep image covers essentially the entire galaxy over a field of radius $R \sim 17'$ (36 kpc at the distance of M101; Table 1), which makes a population study of galactic X-ray sources particularly convenient. The good counting statistics of the image enables us to utilize the high spatial resolution capability ($\sim 5''$ FWHM on-axis) of the instrument, important for resolving X-ray emission both in the galaxy’s central region and in GHCs which are typically located in outer spiral arms of the galaxy. The detection of point-like sources in the image reaches a limiting 0.5-2 keV luminosity of $\sim 4 \times 10^{37}$ ergs s $^{-1}$. The RHRI data also allow for time variability analysis on various time scales. To enhance the long-term timing capability and to characterize spectral properties of the X-ray sources, we have further analyzed archival data from both the *ROSAT* PSPC and the *ASCA* GIS. (The SIS data from the same *ASCA* observation, however, were severely corrupted because of bad telemetry and are not useful.) These X-ray data provide a complementary spatial and spectral coverage over the entire galaxy.

In this paper, we concentrate on discrete X-ray sources in the field of M101. We describe the X-ray observations and data reduction in §2, and catalog X-ray sources in §3. We examine X-ray properties of individual sources (§4) and, in particular, explore the nature of SLS (§5). We statistically characterize the flux distribution of the sources (§6) and its relation to the overall X-ray emission from the galaxy (§7). We further compare our results with observations of X-ray source populations in other nearby galaxies (§8). Finally in §9, we summarize our results and conclusions. In a subsequent paper, we will study the filamentary structure of the diffuse X-ray emission revealed in the RHRI image, will make detailed comparisons with observations in other wavelength bands, and will discuss implications for the structure and evolution of the hot ISM in the galaxy.

2. Observations and Data Calibrations

Table 2 presents a log of main X-ray observations used in the present study. The nominal pointing directions of the *ROSAT* observations were identical: R.A., Dec. (J2000) = $14^h 3^m 9^s.6$, $+54^\circ 20' 24''$, about $0'.65$ southwest of the nucleus of M101 (Table 1). We constructed a single 229 ks RHRI image from 71 individual observing segments included in the 4 observations. We aligned individual segments by matching the centroids of 12 brightest X-ray sources in the field. No offset was found to exceed $6''.5$. A comparison between the co-added radial intensity profiles of point-like sources within $\sim 12'$ off-axis before and after the bore-sight correction shows that the average point response function (PSF) is improved from $9''.5$ to $7''.0$ (FWHM). X-ray sources in the field are, however, not bright enough to allow for correcting potential errors related to the phase of the

telescope wobble.

To obtain an accurate attitude solution of the RHRI image, we compared centroid positions of point-like X-ray sources (H1, H11, H13, H20, H38, H42, and H48; Table 3) with apparent optical counterparts listed in Guide Star Catalog (GSC¹) or in the APM catalog (Irwin, Maddox, & McMahon 1994). We found a satisfactory position alignment by shifting the X-ray images 1".7 to the west and 0".7 to the north and by using a plate scale of 0".499 per pixel (see also Wang 1995).

To reduce the non-cosmic contamination in the RHRI image, we selected only counts within the PHA channel range 2-10. Using a software provided by Steve Snowden, we further obtained both the effective exposure and non-cosmic background maps of the co-added RHRI image. The background-subtracted and exposure-corrected intensity image is shown in Fig. 2.

Complementing the RHRI image, the PSPC observation provided a reasonable spectral resolution of $\delta E/E \sim 0.43(0.93 \text{ keV}/E)^{0.5}$. While both instruments were sensitive to photons in the 0.1-2 keV range, the sensitivity of the PSPC was greater than that of the RHRI, particularly in the 0.1-0.3 keV band. However, the PSPC spatial resolution of about 0'.5 on-axis at ~ 1 keV was substantially lower than that of the RHRI. In the present study, we used only the inner portion of the PSPC observation (Fig. 3) to match the RHRI field of view. This avoided the complication that would be caused by the instrument's supporting ribs at $\sim 20'$ off axis. Based on a comparison with optical counterparts, as in the case of the RHRI image, we obtained a satisfactory attitude solution for the PSPC observation: 5".4 to the east and 9".9 to the north.

The ASCA GIS observation (Fig. 4) covered a broad energy range between 1-10 keV. The spectral resolution of $\delta E/E = 0.078(5.9 \text{ keV}/E)^{0.5}$ was considerably better than the PSPC, although the spatial resolution was poor with an on-axis FWHM of $\sim 1'$ and a 50% half power diameter of $\sim 3'$. A shift of 1'.23 to the north led to a reasonably good match of X-ray source centroids in the ASCA and ROSAT observations.

3. X-ray Source Detection and Catalogs

We searched for X-ray sources in both the PSPC and RHRI images. Following a standard procedure, we conducted local (sliding-box) and map detections as well as final maximum likelihood (ML) analyses of individual sources. We chose the on-source detection aperture as the 90% power-encircled radius of the RHRI PSF, which is a function of off-axis angle. For the RHRI, the radius ranges from 9" on-axis to 44" at 17' off-axis. Both local and map detections were based on the RHRI image with bin size equal to 2".5. To form a smoothed total background map, we first re-binned the RHRI image by a factor of 8 after sources detected in the local detection had been removed. We then applied a median filter to the image with an effective smoothing area

¹version 1.2, see document at [http : //www – gsss.stsci.edu/gsc/gsc12/gsc12_form.html](http://www-gsss.stsci.edu/gsc/gsc12/gsc12_form.html)

of $140'' \times 140''$ around each bin. This smoothing area was large enough for us to neglect statistical uncertainties in the background estimate ($\lesssim 2\%$). The background in source-removed regions was simply the median interpolation from their surroundings. This median filtering effectively removed small-scale ($\lesssim 1'$) features, while keeping the intensity gradient on larger scales. The resultant background map was insensitive to the exact flux threshold for the source removal and was later used to assess the flux limit of the source detection across the field (§6).

In the RHRI image, we found 51 X-ray sources with signal-to-noise ratios greater than 3.5 (Fig. 2). Properties of these sources are summarized in Table 3: RHRI source number (col. 1); right ascension and declination of source centroid (cols. 2 and 3); 1σ error radius (col. 4), including a systematic error of $3''$ estimated from the position dispersion in the attitude solution; signal-to-noise ratio of the detection (col 5); count rate (col 6) corrected for both vignetting and scattering for a point-like source; source energy flux (col 7) converted from the count rate (see below) and corrected for the Eddington bias (Hogg & Turner 1998; §6); and flag on source variability and extent (col. 8).

The conversion from a count rate to an energy flux depends on the spectral shape of a source (Fig. 5). Foreground Galactic stars often have X-ray spectra which can be characterized as optically-thin thermal plasma with temperatures of a few $\times 10^6$ K. AGNs in the *ROSAT* band typically have a power law with a photon index of ~ 2 (e.g., Hasinger et al. 1998). For such spectra, a reasonably good approximation of the conversion is $4 \times 10^{-11} (\text{ergs cm}^{-2} \text{s}^{-1}) / (\text{counts s}^{-1})$ (Fig. 5), which is adopted throughout the paper. The uncertainty should be less than a factor of ~ 2 , except for sources located within or beyond dense clouds with foreground column densities $\gtrsim 2 \times 10^{21} \text{ cm}^{-2}$.

Table 4 lists apparent optical counterparts of 31 X-ray sources. We identified these optical counterparts from spatial cross-correlations of the RHRI sources (Table 3) with objects included in Simbad, GSC, and APM as well as the SNR catalog of M101 (Matonick, & Fesen 1997; MF hereafter). We adopted a matching radius as $2 \times \Delta_{err}$ (Table 3) to keep the candidate of each source unique. Our ongoing spectroscopic observations of X-ray sources in fields of nearby galaxies show that the $B - R$ color of optical counterparts is discriminative: Bright ($B \lesssim 20$) AGNs essentially all have $B - R < 1$ (blue objects), while both galaxies and foreground normal stars typically have $B - R > 1$ (red objects). We classify bright ($R \lesssim 17$ mag) stellar (point-like) red objects as Galactic stars, extended red objects as galaxies, and bright stellar objects with $B - R < 0.8$ as AGNs. Although blue objects could also be white dwarfs in our Galaxy, they would show very soft X-ray spectral characteristics and would then be identified easily.

Table 5 lists 33 PSPC sources detected in the hard band (0.5-2 keV; PI channel 52-201; Snowden et al. 1994). A search in the soft band (PI channel 20-41, centered around 1/4 keV) did not yield any new source, except for a few weak peaks of apparently diffuse X-ray emission; the channels below 20 were not used to avoid the so-called ghost imaging problem. The hardness ratios are defined as $\text{HR1} = (\text{hard} - \text{soft}) / (\text{hard} + \text{soft})$ and $\text{HR2} = (\text{hard2} - \text{hard1}) / (\text{hard2} + \text{hard1})$,

where *soft* and *hard* stand for the net source count rates in the soft and hard bands, while *hard1* and *hard2* are the split of a hard-band rate into two: channel 52-90 (~ 0.75 keV) and 91-201 (~ 1.5 keV). The unphysical values of $HR1 > 1$ for several sources are a result of statistical uncertainties in the data, most serious in the soft band. $HR1$ is particularly sensitive to X-ray absorption, whereas $HR2$ to the intrinsic X-ray spectral shape of a source.

Table 5 also includes the likely RHRI counterparts of individual PSPC sources, based on their position coincidences within the detection apertures. For ease of comparison, both PSPC and RHRI positions of individual sources are marked in Fig. 3. The RHRI image is more sensitive to point-like sources than the much shallower PSPC observation. A considerable number of RHRI sources thus are not detected in the PSPC observation. Also with its limited spatial resolution, the PSPC was unable to resolve several X-ray sources of multiple components in the inner part ($\lesssim 10'$) of the galaxy. Conversely, 3 PSPC sources failed to enter the RHRI source catalog (Table 3). P12, most likely originating in hot ISM of NGC5455, has a very soft spectrum and is apparently extended. The other 2 sources (P3 and P23) are all at large off-axis angles where the PSPC sensitivity is comparatively good.

4. Properties of Individual X-ray Sources

In Tables 3-5, we have included various flags and comments on individual sources. In this session, we systematically describe our spatial, spectral, and timing analyses of the sources.

4.1. Spatial Extent

To identify extended X-ray sources, we compared the count rates detected within the 50% and 90% power-encircled radii around each sources in Table 3 and corrected for scattered fractions (i.e., 50% and 10%). We flagged a source as being likely extended, if the difference of the two rates is greater than 3σ . In the calculation of the count rate uncertainties, we quadratically added to the statistical error of each source a systematic uncertainty of 10% the total count rate (Table 3). This uncertainty was estimated from the count rates of relatively isolated point-like sources (e.g., foreground stars; Table 4). We confirmed the extendness by comparing the average radial intensity profiles of the sources with the expected PSFs. As an example, we show the profile of H23 (M101 nucleus) in Fig. 6. The fit of the PSF to the profile is not acceptable ($\chi^2/n.d.f = 84.1/28$). This extended morphology, together with the soft X-ray spectral characteristics of the source (Table 5), suggests that much of the X-ray emission from the nuclear region arises in diffuse hot gas which emits soft X-rays.

4.2. Spectral Characteristics

The hardness ratios in Table 5 provide a useful spectral characterization of individual sources. Fig. 7 illustrates the dependence of HR1 and HR2 on X-ray-absorbing gas column density and on the parameters of the two spectral models, the power law function and the Raymond & Smith optically thin thermal plasma. The former is typical for AGNs, while the latter is for such galactic sources as stars, SNRs, and superbubbles. The absorption along a line of sight to a foreground star should be less than the total Galactic gas column density (Table 1), while the absorption to an AGN should be a combination of the column densities in the Galaxy and in the M101, typically a few times 10^{20} cm^{-2} total. Complications could arise, though, if a PSPC source consists of multiple components (RHRI sources). Within the PSPC source detection aperture, the calculation of HR1, in particular, may be affected not only by the line-of-sight absorption but also by the presence of diffuse hot gas, which typically has a very soft X-ray spectrum. For example, the abnormal hardness ratio of P21 (both HR1 and HR2 have moderate values) may be a result of a spectral combination between a local diffuse soft X-ray emission enhancement and an SNR embedded in a molecular cloud. Such spectral consideration was included in our classification of the X-ray sources (Tables 4 and 5).

The ASCA GIS image (Fig. 4) maps out the relatively hard X-ray emission above $\sim 1.5 \text{ keV}$. Most noticeable is the absence of emission peaks at locations of several bright *ROSAT* sources: P7 (star), P16 (nuclear region), P25 (GHC), P31 (star), and P32 (SNR), confirming that these sources indeed have very soft X-ray spectra as expected. On the other hand, the GIS image also shows regions of enhanced emission which do not correspond to any features seen in the *ROSAT* images. Particularly notable is the region northwest of the M101 nucleus. An enhancement of X-ray emission in the same region is also present in the IPC image of the galaxy (TFR). The nature of this relatively hard X-ray emission is unclear, although it may represent a couple of X-ray binaries which were absent during the *ROSAT* observations.

4.3. Variability

We tested the variability of each RHRI source in Table 3, using the Kolmogorov-Smirnov statistic. To account for the variability in the non-cosmic X-ray background during the RHRI observations, we constructed a cumulative background count distribution from counts in the RHRI image, excluding regions within the 90% power-encircled radii around individual sources. This background count distribution was normalized to the local background level around each source. The distribution plus a contribution from an assumed constant source flux was then compared with the observed cumulative count distribution within the 90% radii around the source. This comparison shows that 7 sources (H13, H19, H20, H28, H31, H32, and H45) are statistically inconsistent with being constant at the 3σ confidence (probability $P \gtrsim 0.9973$).

We also conducted χ^2 tests for variability in the lightcurves of the RHRI sources. To achieve

reasonable counting statistics, we blocked the lightcurves as 12 ks exposure intervals for sources with individual count rates greater than 10^{-3} counts s^{-1} , and as 20 ks intervals for fainter sources. We determined the time-dependent background by normalizing the total background map of the RHRI image (§2) according to the total source-removed RHRI count rate in each exposure interval. 8 sources (H11, H13, H19, H20, H28, H31, H32, and H45) show significant variabilities, and their light curves are plotted in Fig. 8.

Additional variability information is available from the comparison between the PSPC (hard band) to RHRI count rates in Tables 3 and 5. We assumed a conversion between the two count rates as ~ 3 . But it could reach up to ~ 3.5 for very soft sources, such as foreground stars with little absorption, or down to ~ 2.7 for sources with strong absorption. With this uncertainty in the consideration, 4 PSPC sources (P8, P15, P18, and P28) and 1 RHRI source (H12) appear to vary significantly between the PSPC and RHRI observations. This variability test, however, is problematic for P8, since the point-like RHRI counterpart H10 is embedded within the diffuse X-ray-emitting GHC NGC5447. The count rate discrepancy between the PSPC and RHRI sources may be explained by the difference in the PSFs of the two instruments. The variabilities of other sources are relatively convincing. In fact, during the RHRI observations, both P18 and P28 also exhibited strong variability (Table 3), and P15 (H20) was marginally ($P = 0.9951$) variable.

A comparison with the results from the early IPC observations (TFR) is also interesting. 7 IPC sources (# 1, 2, 4, 5, 6, 7, and 8) are within the field of our consideration. IPC sources 4 and 6 disappeared during the PSPC and RHRI observations. The former was variable between the two IPC observations, and the latter coincided in position with a foreground star.

5. Superluminous X-ray Sources in M101

12 RHRI sources (and more PSPC sources) have fluxes greater than $\sim 3 \times 10^{-14}$ ergs cm^{-2} s^{-1} in the 0.5-2 keV band (Table 3). If associated with M101, such a source has a luminosity of $\gtrsim 2 \times 10^{38}$ ergs s^{-1} in the band; its bolometric luminosity could be much higher and exceeds the Eddington limit for a neutron star with a typical mass of $\sim 1.6M_{\odot}$. Such sources are thus superluminous (SLS or “super Eddington”) and may be good BHCs. Of course, a fraction of these sources (e.g., H1, H6, H11, H20, and H48; Table 3), mostly projected in outskirts of the galaxy, are just interlopers (stars, AGNs, and background galaxies; Table 4). But, as we will show in the next session, there are definitely more such X-ray sources in the M101 field than what is expected in a random field.

SLS in M101 apparently have several origins. 4 PSPC sources (Table 4), which may be classified as SLS, are clearly resolved by the RHRI: P8 into a point-like source (which is still superluminous though) and a diffuse component (NGC5447), P19 into 2 separate sources of comparable fluxes (2 SNR candidates; Wang 1999), P22 into apparently diffuse emission (NGC5461), and P25 into multiple components (NGC5462). Thus at least a fraction of such

sources, especially as seen at low spatial resolution, arises in shock-heated hot gas associated with SNRs and/or GHCs.

Two point-like SLS (H19, and H45) are good candidates for BHCs. Both varied strongly during the RHRI observations (Table 3; Fig. 8). As expected, none of the two sources has an optical counterpart to the APM magnitude limits (see Note to Table 4). However, within its position uncertainty, H19 coincides with an unresolved optical emission line feature, which has been classified as an SNR (Table 4), although their physical relationship is not yet clear. The HR1 values ($\gtrsim 0.8$; Table 5) of the sources indicate large X-ray absorption along the lines of sight. Indeed, the positions of the sources are all projected well within two outer spiral arms of the galaxy (Fig. 1). Therefore, the sources probably represent two high-mass X-ray binaries.

ROSAT observations of other nearby galaxies also suggest that SLS have various origins. A large fraction of them are very young SNRs, in which supernova ejecta are strongly interacting with circumstellar materials. Such sources include SN1986J ($\gtrsim 2 \times 10^{39}$ ergs s $^{-1}$) in NGC891 (Bregman & Pildis 1992), SN1979C ($\sim 1 \times 10^{39}$ ergs s $^{-1}$) in M100 (Immler, Pietsch & Aschenbach 1998), SN1978K (1×10^{39} ergs s $^{-1}$) in NGC1313 (Ryder et al. 1993), and SN1980K ($\sim 3 \times 10^{39}$ ergs s $^{-1}$) in NGC6946 (Canizares, Kriss & Feigelson 1982). Another similarly luminous source in NGC6946 apparently coincides with a young SNR ($\lesssim 3500$ yrs; Schlegel 1994). It is hence conceivable that a fraction of the SLS in M101 is associated with very young SNRs. Other unidentified superluminous X-ray sources tend to be associated with GHCs. One example is the source ($\sim 1 \times 10^{39}$ ergs s $^{-1}$) in NGC4631 (Wang et al. 1995), an interacting galaxy with enhanced star formation. The source is located in a GHC at the border of an HI shell (Vogler & Pietsch 1996). Since the source is found to be variable, it is most likely a high-mass X-ray binary.

It is thus plausible that most, if not all, SLS are related to the formation of very massive stars. In particular, the presence of GHCs is a strong indication for massive starburst activities. GHCs not only power supergiant bubbles of hot gas, but also likely produce various extreme objects, such as black holes and hypernovae (e.g., Paczyński 1998) that can naturally result in super-energetic remnants.

6. Luminosity Distribution of X-ray Sources in M101

To determine the luminosity distribution of X-ray sources in M101, we considered various observational selection effects and accounted for interlopers (e.g., foreground stars and background AGNs) in our X-ray source list (Table 3).

We first approximately corrected for the Eddington bias, caused by the combination of uncertainties in the X-ray flux measurements and the steep flux distribution of the sources. We estimated the “true” (ML) flux as $S = 0.5[1 + (1 - 4\gamma/(s/n)^2)^{1/2}]S_o$ from the observed flux S_o of a source (Hogg & Turner 1998). This correction is significant only for sources near the detection threshold $s/n \sim 3.5$. We thus chose the slope of the flux distribution as $\gamma = 1.94$ (see below). The

correction was applied to each source and to the flux limit of our source detection at each RHRI pixel. The flux limit varied across the field as a function of the PSF size as well as the background and exposure in the RHRI image. Fig. 9 shows the average radial dependence of the flux limit, compared with individual source fluxes.

We then estimated the contribution of interlopers in our source list, based on the differential flux distribution obtained from the *ROSAT* deep surveys (Hasinger et al. 1988). The distribution as a function of the source flux S (0.5-2 keV; in units of 10^{-14} ergs cm^{-2} s^{-1}) has a form $n_b(S) = n_{b,0} S^{-\gamma_b}$, where $n_{b,0} = 238.1$ and $\gamma_b = 2.72$ for $S > 2.66$, or 111.0 and 1.94 for $S < 2.66$, respectively. We integrated the function to obtain the expected contribution above our source detection flux limit at each pixel of the RHRI image. Fig. 10 shows the contribution as a function of galactocentric radius R of M101. The excess of the source density above the interloper contribution decreases with increasing R . In the $R \lesssim 12'$ region, where variation in the flux limit is relatively small (Fig. 9), the number of estimated interlopers is 19.7, and 21.3 ± 6.4 sources are expected to be associated with M101. Most interesting is an excess of sources with $S \gtrsim 3$ within the $R = 5' - 12'$ annulus: 8 such sources compared to the expected 2.6 interlopers. This excess is significant at the confidence of 99.8%. In comparison, no such sources are at smaller R in the RHRI image. Between $R = 12' - 17'$ the observed number of sources with $S \gtrsim 3$ is 4, compared to the expected 2.7. Thus the excess is statistically insignificant. Indeed, 3 of the 4 sources are identified (Table 4): H1 and H20 as foreground stars, and H51 as a background galaxy. While the excess of sources is most significant in the $R \lesssim 5'$ region, they all have $S \lesssim 3$. In contrast, no significant difference is found between the observed and the expected number of sources with $S \lesssim 3$ in the $R \gtrsim 5'$ region.

We next parameterized the flux distribution of the M101 sources as a power law function: $n(S) = n_o S^{-\gamma}$. Using this function and the above broken power law for interlopers, we conducted an ML fit (e.g., Cash 1980) to the fluxes of the 41 RHRI sources with $R \leq 12'$. This fit gave $\gamma = 1.9(1.6 - 2.4)$ (90% confidence interval). The effect of the Eddington correction on γ is considerable ($\sim 15\%$), but is still smaller than the statistical uncertainty. As a function of γ , the normalization is $n_o = 105(79 - 128)$. The fit is satisfactory with the V_e/V_a statistic (Avni & Bahcall 1980) equal to 0.51, compared to the expected value of $0.5 \pm 0.045(1\sigma)$. Fig. 11 compares the flux distribution of the sources with the best-fit model.

The power-law function can be readily converted into the average luminosity distribution of M101 sources: $dN/dL_x \equiv N_o L_x^{-\gamma}$, where $N_o = 9.5(8.0 - 9.7)$ sources per 10^{38} ergs s^{-1} in the 0.5-2 keV band. Including the Poisson uncertainty in the total number of the sources, we obtain $N_o = 9.5(4.0 - 14)$.

The luminosity distribution may, however, vary with R . As noted earlier, there is a clear excess of $S \gtrsim 3$ sources in the $R = 5' - 12'$ annulus. The number of lower flux sources is comparatively small. An ML fit to sources in the annulus only gives $\gamma = 1.7(1.4 - 2.2)$, which is considerably smaller than the above value for the entire $R \leq 12'$ region. In contrast, the central

region contains 16 sources in the $S \sim 0.4 - 3$ range, but no source with $S \gtrsim 3$. The expected number ratio $N(S \gtrsim 3)/N(0.4 \lesssim S \lesssim 3)$ is 0.16, assuming $\gamma = 1.9$, and greater if $\gamma \sim 1.7$ is used. The probability for detecting no source in the $S \gtrsim 3$ range is thus $\lesssim 0.073$. Unfortunately, both the flux range and the number statistics of the sources in the central region are too small to constrain effectively an independent luminosity distribution. Nevertheless, the above analysis indicates that the central region intrinsically lacks SLS and that the luminosity distribution depends on R . This radial dependence may be related to the large metallicity gradient observed in the galaxy (a factor of 10 decrease from the galactic center to outskirts; e.g., Kennicutt & Garnett 1996; Torres-Peimbert, Peimbert, & Fierro, 1989). Massive stars with low metallicity may be relatively inefficient in losing mass, and may more likely end their life as hypernovae (e.g., Paczyński 1998) and form black holes than stars with high metallicity. This metallicity effect may partly explain why no persistent SLS have been observed in such early-type spirals as M31 and our own Galaxy, both of which have relatively high metal abundances (§8).

7. Overall X-ray Emission from M101

In addition to the detected sources, as listed in Tables 3 or 5, there are large amounts of low-surface brightness X-ray emission associated with M101. Fig. 12 shows an RHRI intensity map that has been adaptively smoothed to emphasize this emission. After both excising individual sources within their 90% power-encircled radii and subtracting a background calculated in the annulus of $R = 12' - 15'$, we estimated the excess of the “diffuse” X-ray emission as 0.028 counts s^{-1} in the $R \leq 5'$ region and 0.02 counts s^{-1} in the $R = 5' - 12'$ annulus. In comparison, the total count rate of the sources in the same regions are 0.0052 and 0.012 counts s^{-1} , including the contribution from interlopers. Clearly the fractional contribution from the sources is substantially greater in the annulus than in the central region, although our source detection flux limit is higher in the former than in the latter. The total 0.5-2 keV luminosity of the diffuse emission within $R = 12'$ is $\sim 9 \times 10^{39}$ ergs s^{-1} .

Can discrete sources just below our source detection limit explain the apparently diffuse X-ray emission? Indeed, a modest extrapolation of the average luminosity distribution of M101 sources (§6) may reasonably account for the excess flux in the $R = 5' - 12'$ annulus. To explain the flux in the $R \leq 5'$ region, however, $\gamma \gtrsim 2$ is required. For $\gamma = 2$, for example, the extrapolation needs to reach $L_x \sim 7 \times 10^{34}$ ergs s^{-1} , which is substantially smaller than the typical luminosity of an X-ray binary system ($L_x \gtrsim 10^{36}$ ergs s^{-1}). As argued by Snowden & Pietsch (1995), other less luminous types of X-ray sources (e.g., M dwarfs and white dwarf accretion binaries) are also unlikely to account for the bulk of the X-ray emission from the central region of the galaxy. Therefore, the central region probably contains truly diffuse X-ray emission.

To further explore the nature of the X-ray emission from the central region, we studied spectral data from both the PSPC and GIS observations. We extracted the data from the $R \leq 5'$ region and estimated the background contribution from an annulus of $R \sim 12' - 15'$. Because the

limited spatial resolution of the data, we did not attempt to remove the sources. We obtained satisfactory joint fits to the PSPC and GIS spectra (Fig. 13), assuming the two-component models as listed in Table 6. Both models give a 0.1-10 keV luminosity as $\sim 2.0 \times 10^{40}$ ergs s $^{-1}$. The high temperature thermal plasma (or the power law component) alone predicts an RHRI count rate of ~ 0.01 counts s $^{-1}$, or about twice the total detected source count rate in the region. Thus it is reasonable to assume that this component arises in discrete sources, most of which may be X-ray binaries in the luminosity range of $10^{36} - 10^{38}$ ergs s $^{-1}$ and tend to have relatively hard X-ray spectra. The low-temperature component is likely dominated by truly diffuse hot gas. The characteristic temperature is even lower than that (0.26-0.60 keV) of diffuse hot gas observed in the Large Magellanic Cloud (Wang et al. 1991; Trümper et al. 1991; Snowden & Petre 1995). This is, at least partly, due to the high gas column density ($N_{HI} \sim 6 \times 10^{20}$ cm $^{-2}$ in our Galaxy alone) toward the LMC; very soft ($\lesssim 0.3$ keV) X-rays are severely absorbed, which biases the detection to gas at temperatures $\gtrsim 0.3$ keV in the Cloud. There might be an even cooler (a few times 10^5 K) gas component in M101. The best-fit N_H in Table 6 is considerably smaller than the expected Galactic column density (Table 1). This is an indication for the presence of a very soft component in the spectral data (Wang et al. 1995), although the quality of the data used here is not good enough to quantify this spectral component.

We have further found that the diffuse X-ray emission is strongly correlated with HII regions in M101. Thus as in the LMC (Wang et al. 1991), we expect that the X-ray emission is dominated by hot gas heated by a combination of supernova blastwaves and stellar winds from massive stars. We will explore the implications of this correlation further in a later paper.

8. Comparison with Other Nearby Spiral Galaxies

We concentrate here on the comparison of M101 with 6 other nearby spiral galaxies that we are familiar with. Table 7 lists the salient parameters of these galaxies, arranged according to their far-infrared (FIR) luminosities (L_{FIR}). The galaxies cover a good range of morphological type, H I mass, and star forming rate. The X-ray results are all based on *ROSAT* observations. Because we are mostly interested in the overall galactic X-ray properties, the contributions from nuclear X-ray sources are excluded from both Table 7 and Fig. 14, where the X-ray source luminosity distributions of the galaxies are compared. In addition, SN1979C of M100 is not included. This bright SN ($L_x = 10^{39}$ ergs s $^{-1}$) would have been detected in all other galaxies in many wavelength regimes. Furthermore, all identified interlopers are removed for each galaxy, according to the referenced papers (Table 7). But the data quality and analysis differ significantly from one galaxy to another, which might cause errors in our calculation of the luminosity distributions, particularly in the lowest or the highest luminosity bins. The lowest luminosity bins are affected chiefly by uncertainties in source detection thresholds and in various source confusions, most seriously in PSPC observations, while the highest luminosity bins by the uncertainty in removing interlopers. The intermediate luminosity bins should be relatively reliable. The galaxies seem to have very

similar H I mass-normalized X-ray source luminosity distributions (within current measurement errors), although the high luminosity cutoffs can be very different.

Both the X-ray luminosity and the number of SLS appear to be correlated with its *total* star forming rate, as traced by the L_{FIR} of a galaxy (Table 7). The three galaxies (M33, M31, and NGC253) with the lowest L_{FIR} also have the lowest L_{x} and N_{SLS} , whereas the three galaxies (M51, M100, M83) with the highest L_{FIR} also have the highest L_{x} and N_{SLS} . In terms of these properties, M101 is just intermediate among the galaxies listed in Table 7.

9. Summary

We have carried out a comprehensive study of X-ray sources in the field of M101. We detected 51 sources in an ultradeep RHRI image and additional 3 sources in a PSPC observation. We have examined spatial, spectral, and timing properties of these sources as well as characteristics of their optical counterparts (magnitude, color, and extent). We have also investigated the statistical properties of the sources and their relationship to the overall X-ray emission from the galaxy. Furthermore, we have compared this study with works on other nearby galaxies. The major results and conclusions are as follows:

- Significant X-ray emission is detected from M101 over a region of $R \sim 25$ kpc from the galaxy’s nucleus. The total luminosity is $\sim 1 \times 10^{40}$ ergs s $^{-1}$ in the 0.5-2 keV band.
- 16 sources are identified as interlopers: 8 as foreground stars, 3 as background galaxies, and 5 as AGNs (Tables 4 and 5). Unidentified interlopers (~ 10) are most likely AGNs, which are relatively faint in optical.
- About 25 sources are associated with M101, which are in the luminosity range of $L_{\text{x}} \sim (4 - 200) \times 10^{37}$ ergs s $^{-1}$.
- The 5 brightest GHCs in M101 all show strong X-ray emission (Table 5): 4 of them (NGC5447, NGC5455, NGC5461, and NGC5462; Fig. 12) are clearly resolved, which most likely contain hot gas emitting diffuse soft X-rays; The emission from NGC5471 is likely dominated by a hypernova remnant (Wang 1999), which is also unusually bright in optical and radio (Yang et al. 1994; Chen & Chu 1999). The diffuse emission from the GHCs will be discussed further in a separate paper.
- Additional 4 position coincidences are found between X-ray sources and previously classified SNRs in the galaxy. Some of these coincidences, however, may result from superpositions by chance. The observed X-ray luminosities, if arising in blastwave-heated gas, suggest that these remnants originate in explosions much more energetic than typical supernovae. A thorough discussion of such remnants in M101 has been given by Wang (1999).

- SLS, with luminosities significantly greater than the Eddington limit for a neutron star, are located exclusively in outer regions ($R \gtrsim 10$ kpc) of the galaxy. We identify 2 variable SLS as candidates for X-ray binary systems with black holes. These sources show highly-absorbed X-ray spectral characteristics and are apparently embedded in spiral arms, indicating massive star origins.
- The average luminosity distribution of M101 sources is parameterized as a power law function: $dN/dL_x = N_o L_x^{-\gamma}$ with $\gamma = 1.9(1.6 - 2.4)$ and $N_o = 9.5(4.0 - 14)$ sources per 10^{38} ergs s^{-1} (90% confidence intervals). However, the luminosity distribution may be a function of galactocentric radius. In particular, X-ray sources in the central region appear to have an upper luminosity cutoff at $L_x \sim 2 \times 10^{38}$ ergs s^{-1} .
- The detected sources account for only $\sim 16\%$ of the X-ray emission observed in the central $R \lesssim 10$ kpc region. A substantial fraction of the residual emission likely arises in the hot ISM at a characteristic temperature of $\sim 2 \times 10^6$ K.
- Comparison of X-ray properties of 7 nearby spirals suggests that both the X-ray luminosity and the number of SLS are correlated with the galactic star forming rate. However, except for the different upper luminosity cutoffs, nearby spirals seem to have very similar X-ray source luminosity functions (after being normalized by the total H I masses of the galaxies).

We thank the referee for comments that led to improvements of the presentation of the paper. This research made use of various online services and databases (e.g., HEASARC website, Simbad, NED, APM, and DSS). Q.D.W. is supported by NASA (grant NAG 5-3414 and NAG5-6413). The ROSAT project at MPE is supported by the German Bundesministerium für Bildung, Wissenschaft, Forschung und Technologie (BMBF/DLR) and the Max-Planck-Gesellschaft (MPG).

REFERENCES

- Avni, Y., & Bahcall, J. N. 1980, *ApJ*, 235, 694
- Bregman, J. N., & Pildis, R. A. 1992, *ApJL*, 398, 107
- Canizares, C., Kriss, G. A., & Feigelson, E. D. 1982, *ApJL*, 253, 17
- Cash, W. 1979, *ApJ*, 228, 939
- Chen, C.-H. R., & Chu, Y.-H. 1999, *BAAS*, 193, 7405
- David, L. P., et al. 1996, *The ROSAT Users Handbook*, eds: U. G. Briel, et al.
- de Vaucouleurs, G., de Vaucouleurs, A., Corwin, H., Jr., Buta, R., Paturel, G., & Fouqu, P. 1991, *Third Reference Catalogue of Bright Galaxies* (Berlin: Springer)

- Devereux, N. A., & Eales, S. A. 1989, *ApJ*, 340, 708
- Dickey, J. M., & Lockman, F. J. 1990, *ARA&A*, 28, 215
- Ehle, M., Pietsch, W., & Beck, R. 1995, *A&A*, 295, 289
- Ehle, M., Pietsch, W., Beck, R., & Klein, U. 1998, *A&A*, 329, 39
- Fabbiano, G. 1998, *The Hot Universe (IAU Sym. No.188.)*, eds: K. Koyama, S. Kitamoto, & M. Itoh. Dordrecht : Kluwer Academic, p93
- Hasinger, G., Burg, R., Giacconi, R., Schmidt, M., Trümper, J., & Zamorani, G. 1998, *A&A*, 329, 482
- Hogg, D. W., & Turner, E. L., 1998, *PASP*, 110, 727
- Immler, S., Pietsch, W., & Aschenbach, B. 1998, *A&A*, 331, 601
- Irwin, M., Maddox, S., & McMahon, R. 1994, *Spectrum*, 2, 14
- Israel, F. P., Goss, W. M., & Allen, R. J. 1975, *A&A*, 40, 421
- Kennicutt, R. C., Jr., & Garnett, D. R. 1996, *ApJ*, 456, 504
- Long, K., & Van Speybroeck, L. P. 1983, *Accretion-Driven Stellar X-ray Sources*, ed. W. H. G. Lewin, & P. J. Van Den Heuvel
- Matonick, D. M., & Fesen, R. A. 1997, *ApJS*, 112, 49 (MF)
- McCammon, D., & Sanders, W. T. 1984, *ApJ*, 287, 164
- Paczyński, B. 1998, *ApJL*, 494, 45
- Pfeffermann, E., et al. 1987, *Proc. SPIE Int. Soc. Opt. Eng.*, 733, 519 (Cambridge: Cambridge Univ. Press), p117
- Read, A., Ponman, T. J., & Strickland, D. K. 1997, *MNRAS*, 286, 626
- Rice, W., et al. 1988, *ApJS*, 68, 91
- Ryder, S. D., et al. 1993, *ApJ*, 416, 167
- Sandage, A., & Tammann, G. 1981, *Revised Shapley-Ames Catalog of Bright Galaxies* (Washington: Carnegie)
- Schlegel, E. M. 1994, *ApJL*, 424, 99
- Schulman, E., & Bregman, J. N. 1995, 441, 568
- Snowden, S. L., McCammon, D., Burrows, D. N., & Mendenhall, J. A. 1994, *ApJ*, 424, 714
- Snowden, S. L., & Petre, R. 1994, *ApJL*, 436, 123
- Snowden, S. L., & Pietsch, W. 1995, *ApJ*, 452, 627
- Soifer, B. T., Boehmer, L., & Neugebauer, G. 1989, *AJ*, 98, 766
- Stark, A. A., et al. 1992, *ApJS*, 79, 77
- Stetson, P. B. et al. 1998, *ApJ*, 508, 491

- Supper, R., et al. 1997, A&A, 317, 328
- Torres-Peimbert, S., Peimbert, M., & Fierro, J. 1989, ApJ, 345, 1
- Trinchieri, G., Fabbiano, G., & Romaine, S. 1990, ApJ, 356, 110 (TFR)
- Trümper, J., et al. 1991, Nature, 349, 583
- Tully, R. B. 1988, Nearby galaxies catalog, Cambridge University Press, Cambridge and New York.
- Vogler, A., & Pietsch, W. 1996, A&A, 331, 35
- Wang, Q. D. 1995, ApJ, 453, 783
- Wang, Q. D. 1999, ApJL, 517, May 20 issue
- Wang, Q. D., Hamilton, T. T., Helfand, D. J., & Wu, X. 1991, ApJ, 374, 475
- Wang, Q. D., & Helfand, D. J. 1991, ApJ, 379, 327
- Wang, Q. D., Walterbos, R., Steakley, M. F., Norman, C. A., & Braun, R. 1995, ApJ, 439, 176
- Williams, R., & Chu, Y.-H. 1995, ApJ, 439, 132
- Yang, H., Skillman, E. D., & Sramek, R. A. 1994, AJ, 107, 651
- Zaritsky, D., Elston, R., & Hill, J. M. 1990, AJ, 99, 1108

Fig. 1.— Optical image of M101 from Palomar Sky Survey. RHRI sources (\square) and three additional sources (\diamond), detected only in the PSPC observation, are marked.

Fig. 2.— RHRI intensity contour map of M101 and RHRI sources. The map is adaptively smoothed with a Gaussian with size adjusted to achieve a constant signal-to-noise ratio of ~ 4 . The contours are at 1.4, 2.1, 3.3, 6.5, 16, and 39×10^{-3} counts $\text{s}^{-1} \text{ arcmin}^{-2}$; the lowest level is about 3σ above the local X-ray background. Both positions (+) and catalog numbers of the sources (Table 3) are marked.

Fig. 3.— PSPC 0.5-2 keV band image of M101. The PSPC intensity map is smoothed in the same way as the RHRI map in Fig. 2, and the contours are at 1.2, 1.8, 2.9, 5.6, 14, and 33×10^{-3} counts $\text{s}^{-1} \text{ arcmin}^{-2}$. Both positions (\times) and catalog numbers of PSPC sources (Table 5) are marked. For ease of comparison, the positions of RHRI sources (+) are also included.

Fig. 4.— 1.5-10 keV band image of M101 from the ASCA GIS. The GIS intensity map is smoothed in the same way as the RHRI map in Fig. 2, and the contours are at 2.0, 2.6, 3.5, 4.7, 6.2, and 8.0×10^{-4} counts $\text{s}^{-1} \text{ arcmin}^{-2}$. The positions of RHRI sources (+) are marked.

Fig. 5.— Conversion factor (in units of $10^{-11} \text{ ergs cm}^{-2} \text{ s}^{-1} / \text{ counts s}^{-1}$) of an RHRI count rate to an unabsorbed (absorption-free) flux in the 0.5-2 keV band as a function of model parameters. The thick curves are for power law with photon index of 1 (solid), 2 (dotted), and 3 (dashed), while the thin curves are for Raymond & Smith plasma with $kT = 0.2$ (solid), 0.4 (dotted), and 1 keV (dashed), respectively.

Fig. 6.— Radial RHRI intensity profile around the M101 nucleus, compared to the PSF of the instrument (the solid curve).

Fig. 7.— Dependency of PSPC hardness ratios on X-ray-absorbing gas column density and on spectral model parameters. The set of dashed curves is for HR1, while the set of solid curves is for HR2. In (A), the three curves (from the bottom to the top) of each set are for the power law model with photon index equal to 1, 2, and 3. In (B), the 5 solid curves (from the bottom to the top) are for the Raymond & Smith plasma with temperature equal to 0.1, 0.2, 0.5, 1, and 2 keV, while the order for the 5 dashed curves are 0.1, 0.2, 2, 1, and 0.5 keV. The metal abundances of both X-ray-emitting and -absorbing materials are assumed to be the solar.

Fig. 8.— Light-curves of 9 RHRI sources which show significant variability. The error bars of the data points are at the 1σ confidence. The reduced χ^2 value as well as the variability significance and source number are given on the right side of each panel. The dotted lines represents the mean count rates over the four individual observation blocks, which are separated by several months, while the dashed line indicates the mean count rate over the complete observation.

Fig. 9.— Comparison of RHRI source fluxes and the detection limit. The solid curve represents the flux limit calculated with an azimuthally-averaged radial background intensity profile, while the dashed curves assume the background profile plus or minus $3\times\text{rms}$.

Fig. 10.— Number distribution of X-ray sources. The data points and 1σ error bars are from the detected RHRI sources (Table 3). The solid curve shows the estimated contribution from interlopers. The dashed curve represents the contribution that assumes both an average flux distribution of sources within $R = 12'$ and a uniform surface source density.

Fig. 11.— X-ray flux distribution of RHRI sources within $R = 12'$. The units of the source density is the number of sources per 10^{-14} ergs cm^{-2} s^{-1} (0.5-2 keV) and per degree². The horizontal bars represent the flux ranges of individual data point, whereas the vertical bars represent the square root of the observed source numbers (chosen to be 6, except for the highest flux range). The lower flux range extends to the minimum detection limit of the field. The upper limit of the highest flux range is arbitrarily selected to be the highest observed source flux; thus the density of the range is likely overestimated. The ML fit was performed on the data of individual sources without the binning. The best-fit model (M101 sources plus interlopers) is shown as the solid (intrinsic) and dashed (flux limit-corrected) curves. The thin curves represent the best-fit contribution from M101 only.

Fig. 12.— RHRI intensity map of the inner part of M101, adaptively smoothed with a constant signal-to-noise ratio of ~ 6 . The contours are at 1.1, 1.3, 1.7, 2.2, 3, 4, 6, 12, 24, 48, and 100×10^{-3} counts s^{-1} arcmin⁻².

Fig. 13.— PSPC and GIS spectra of the inner $R \leq 5'$ region around the nucleus of M101. The histograms represent the best-fit two-temperature thermal plasma model (Table 6), while the lower panel shows the residual of the fit.

Fig. 14.— A comparison of X-ray source luminosity distributions of nearby spirals (see also Table 7).

This figure "fig1.gif" is available in "gif" format from:

<http://arxiv.org/ps/astro-ph/9903479v1>

This figure "fig2.gif" is available in "gif" format from:

<http://arxiv.org/ps/astro-ph/9903479v1>

This figure "fig3.gif" is available in "gif" format from:

<http://arxiv.org/ps/astro-ph/9903479v1>

This figure "fig4.gif" is available in "gif" format from:

<http://arxiv.org/ps/astro-ph/9903479v1>

This figure "fig5.gif" is available in "gif" format from:

<http://arxiv.org/ps/astro-ph/9903479v1>

This figure "fig6.gif" is available in "gif" format from:

<http://arxiv.org/ps/astro-ph/9903479v1>

This figure "fig7a.gif" is available in "gif" format from:

<http://arxiv.org/ps/astro-ph/9903479v1>

This figure "fig7b.gif" is available in "gif" format from:

<http://arxiv.org/ps/astro-ph/9903479v1>

This figure "fig8.gif" is available in "gif" format from:

<http://arxiv.org/ps/astro-ph/9903479v1>

This figure "fig9.gif" is available in "gif" format from:

<http://arxiv.org/ps/astro-ph/9903479v1>

This figure "fig10.gif" is available in "gif" format from:

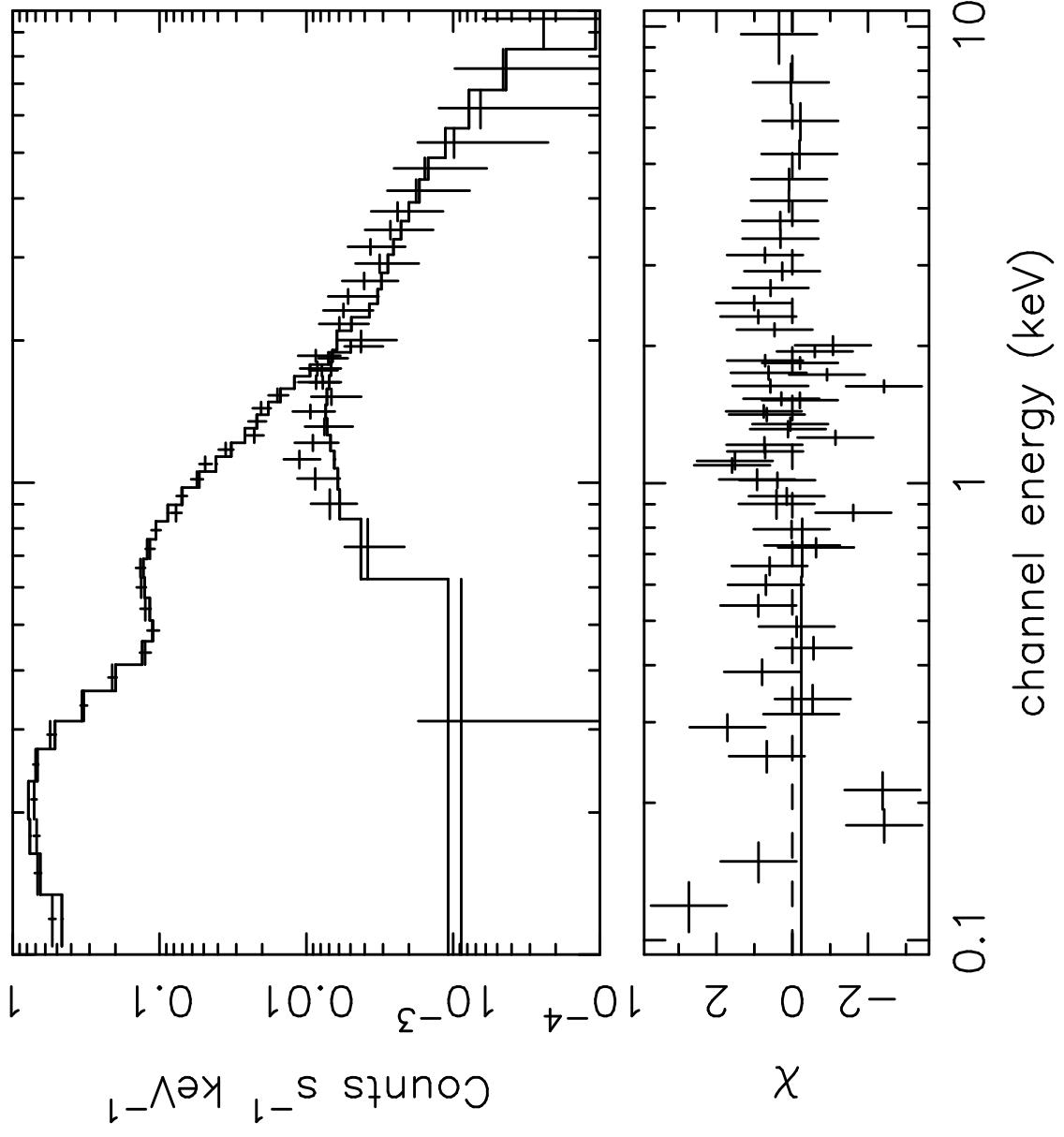
<http://arxiv.org/ps/astro-ph/9903479v1>

This figure "fig11.gif" is available in "gif" format from:

<http://arxiv.org/ps/astro-ph/9903479v1>

This figure "fig12.gif" is available in "gif" format from:

<http://arxiv.org/ps/astro-ph/9903479v1>



This figure "fig14.gif" is available in "gif" format from:

<http://arxiv.org/ps/astro-ph/9903479v1>

Table 1: Parameters of M101

Type	Sc(s) or SAB(rs)cd	Sandage & Tammann (1981) de Vaucouleurs et al. (1991)
Distance	7.2 ± 0.5 Mpc ($1' = 2.1$ kpc)	Stetson et al. (1998)
Galactic nucleus position (J2000)	R.A. = $14^h 3^m 12^s.7$ Dec. = $+54^\circ 20' 54''.2$	Israel, et al. (1975)
R_{25} radius	13.5 kpc	de Vaucouleurs et al. (1991)
Disk inclination	17°	Zarisky et al. (1990)
Galactic N_H	$1.1 \times 10^{20} \text{ cm}^{-2}$	Stark et al. (1992)

Table 2: X-ray Observations Log of M101

Instrument	Seq. No.	Date	Exposure
ROSAT RHRI	rh600092n00	92 Jan 9 - Jan 11	18.4 ks
ROSAT RHRI	rh600383n00	92 Dec 10 - Dec 14	32.6 ks
ROSAT RHRI	rh600820n00	96 May 14 - Jun 9	107.9 ks
ROSAT RHRI	rh600820a01	96 Nov 21 - Nov 23	68.2 ks
ROSAT PSPC	rp600108n00	91 Jun 8 - Jun 9	34.5 ks
ASCA GIS	ad61017000	94 May 2	19.9 ks

Table 3: RHRI Sources in the M 101 Field

RHRI Source	R.A.(J2000) (h m s)	Dec.(J2000) (^o ' ")	Δ_{err} (")	s/n	CR (cts ks ⁻¹)	$S(0.5-2 \text{ keV})$ (ergs cm ⁻² s ⁻¹)	Var. & Ext. ^a
(1)	(2)	(3)	(4)	(5)	(6)	(7)	(8)
H 1	14 1 19.1	54 18 40	3.4	21.2	5.43	21.63E-14	
H 2	14 1 23.9	54 15 19	6.9	5.2	1.04	3.83E-14	
H 3	14 2 03.2	54 18 28	3.3	7.3	0.58	2.23E-14	
H 4	14 2 06.5	54 17 09	4.1	3.9	0.26	0.89E-14	
H 5	14 2 07.7	54 10 30	4.5	6.0	0.71	2.68E-14	
H 6	14 2 10.2	54 30 19	5.0	4.7	0.53	1.91E-14	
H 7	14 2 13.4	54 21 57	3.8	3.6	0.20	0.65E-14	
H 8	14 2 13.7	54 23 07	3.8	3.6	0.21	0.69E-14	
H 9	14 2 21.9	54 17 57	3.1	9.1	0.64	2.50E-14	
H10	14 2 27.8	54 16 26	3.0	15.6	1.49	5.91E-14	
H11	14 2 27.9	54 12 42	3.1	13.8	1.37	5.42E-14	
H12	14 2 28.3	54 26 31	3.2	8.2	0.59	2.29E-14	PH _v
H13	14 2 29.5	54 21 19	3.0	23.9	3.14	12.52E-14	H _v
H14	14 2 32.0	54 20 01	3.2	5.4	0.29	1.08E-14	
H15	14 2 34.2	54 21 18	3.3	4.1	0.20	0.69E-14	
H16	14 2 46.2	54 21 51	3.3	3.9	0.19	0.65E-14	
H17	14 2 46.6	54 26 55	3.3	5.9	0.34	1.28E-14	
H18	14 2 52.5	54 21 12	3.1	7.2	0.42	1.62E-14	
H19	14 3 03.7	54 27 36	3.0	22.7	2.78	11.08E-14	H _v
H20	14 3 03.9	54 04 04	4.6	9.4	2.21	8.64E-14	H _v
H21	14 3 05.8	54 07 12	4.9	5.0	0.58	2.13E-14	
H22	14 3 12.2	54 17 58	3.2	4.5	0.22	0.79E-14	
H23	14 3 12.4	54 20 54	3.0	9.8	0.67	2.62E-14	ext
H24	14 3 12.9	54 20 08	3.2	4.9	0.26	0.95E-14	ext
H25	14 3 13.9	54 18 05	3.3	4.0	0.19	0.65E-14	
H26	14 3 17.6	54 18 21	3.2	4.8	0.24	0.87E-14	
H27	14 3 18.5	54 24 32	3.4	3.8	0.18	0.60E-14	
H28	14 3 19.2	54 17 18	3.2	5.1	0.26	0.96E-14	H _v
H29	14 3 21.3	54 19 46	3.1	8.7	0.56	2.18E-14	ext
H30	14 3 23.9	54 19 47	3.1	7.7	0.47	1.82E-14	ext
H31	14 3 30.8	54 21 57	3.4	3.5	0.18	0.58E-14	H _v , PH _v
H32	14 3 32.3	54 21 03	3.1	5.8	0.32	1.20E-14	H _v , PH _v
H33	14 3 33.2	54 17 59	3.2	4.3	0.21	0.74E-14	
H34	14 3 34.1	54 11 48	4.1	3.5	0.23	0.74E-14	
H35	14 3 35.2	54 17 08	3.2	4.6	0.23	0.83E-14	
H36	14 3 35.7	54 19 24	3.1	7.8	0.49	1.90E-14	
H37	14 3 40.9	54 19 03	3.2	5.6	0.31	1.16E-14	ext
H38	14 3 50.4	54 24 13	3.2	6.4	0.38	1.44E-14	
H39	14 3 51.6	54 21 47	3.3	4.5	0.24	0.86E-14	
H40	14 3 53.7	54 21 57	3.1	9.7	0.69	2.70E-14	
H41	14 3 55.3	54 21 32	3.5	3.6	0.18	0.59E-14	
H42	14 3 55.9	54 20 58	3.4	4.0	0.21	0.72E-14	
H43	14 3 59.1	54 09 13	5.4	4.4	0.51	1.81E-14	
H44	14 4 00.3	54 11 32	4.2	5.1	0.44	1.62E-14	
H45	14 4 14.1	54 26 04	3.0	34.8	7.10	28.35E-14	H _v
H46	14 4 15.2	54 09 44	5.7	4.8	0.67	2.43E-14	
H47	14 4 16.5	54 16 13	3.3	9.2	0.84	3.28E-14	
H48	14 4 21.6	54 19 21	3.1	15.0	1.70	6.74E-14	
H49	14 4 29.0	54 23 52	3.4	10.6	1.22	4.79E-14	
H50	14 4 39.4	54 26 53	7.5	3.5	0.50	1.62E-14	
H51	14 4 55.9	54 24 04	7.3	4.6	0.85	3.05E-14	

^a H_v - variable in RHRI observations; PH_v - variable between the PSPC and RHRI observations; Ext - extended.

Table 4: Optical Counterparts of the RHRI Sources^a

RHRI Source	offset (")	<i>R</i> (mag)	<i>B</i> (mag)	<i>B</i> − <i>R</i> (mag)	Identification & Comments ^b
H 1	6.4	11.09	13.13	2.04	star GSC738
H 2	8.2	—	21.86	≤1.86	stellar object
H 4	3.2	—	21.23	—	non-stellar object
H 6	8.5	18.57	19.28	0.71	AGN; Note
H11	5.0	14.89	17.31	2.42	star
H12	4.0	—	21.58	—	non-stellar object
H13	4.1	14.83	—	—	star GSC1275; Note
H15	5.6	18.08	—	≥2.92	star
H17	4.5	19.30	21.08	1.78	galaxy
H18	4.3	—	20.39	≤0.39	AGN; Note
H19	3.3	—	—	—	XB, SNR MF37
H20	9.1	15.97	19.03	3.06	star
H23	2.1	—	—	—	M101 nucleus; Note
H28	3.0	19.78	—	—	Note
H29	6.3	—	—	—	SNR MF54
H30	4.0	—	—	—	SNR MF57
H32	2.6	—	21.13	≤1.13	stellar object
H33	5.7	18.23	20.26	2.03	non-stellar object
H35	2.9	—	21.10	≤1.10	stellar object
H36	1.8	—	—	—	SNR MF83
H37	1.4	8.84	10.85	2.01	NGC5461
H38	1.6	19.98	20.93	0.95	AGN; Note
H40	4.0	—	9.81	—	NGC5462
H42	2.7	15.46	18.39	2.93	star
H44	2.7	19.21	19.80	0.59	AGN; Note
H46	5.7	—	21.13	≤1.13	stellar object
H47	3.0	18.66	19.53	0.87	AGN; Note
H48	0.6	10.91	12.68	1.77	star GSC1062, AG10
H49	3.1	—	—	—	SNR NGC5471B
H50	3.7	19.22	20.66	1.44	red stellar object
H51	7.4	11.83	14.72	2.89	galaxy

^a The *B* and *R* refer to the internally calibrated red and blue plate catalogue magnitudes on an approximately real magnitude scale (Irwin et al. 1994). For stellar (point-like) objects, colors are consistent to ± 0.25 mag. The calculation of *B* − *R* limits assumes the limiting magnitude 21.5 mag for the Palomar O (blue) plates and 20 mag for the E (Red) plate.

^b star - foreground star in the Galaxy. Additional notes to individual sources: H6, H18, H38, H44, and H47 - These blue stellar objects all have large HR1 values (Table 5), suggesting that they are not white dwarfs and are most likely AGNs. H13 - Detection in the O plate is confused with a nearby object. H23 - extended in both optical and X-ray. H28 - blended objects within a spiral arm.

Table 5: PSPC Sources

PSPC Source	R.A. (h m s)	Dec. ($^{\circ}$ ' ")	s/n	CR (cts ks $^{-1}$)	Hardness Ratio		Other Name	Identification & Comment ^a
					HR1	HR2		
P 1	14 1 19.6	54 18 41	16.9	16.2	0.34 \pm 0.05	0.03 \pm 0.06	H1,TFR1	star
P 2	14 1 23.4	54 15 28	5.7	3.0	0.10 \pm 0.14	0.27 \pm 0.18	H2	
P 3	14 1 34.6	54 20 32	7.3	3.8	0.85 \pm 0.16	0.12 \pm 0.13		galaxy: $R = 16.7, B = 18.7$
P 4	14 2 03.1	54 18 32	4.8	1.7	1.38 \pm 0.42	0.16 \pm 0.20	H3	
P 5	14 2 10.7	54 30 30	5.6	2.5	0.55 \pm 0.17	0.39 \pm 0.16	H6	AGN
P 6	14 2 22.2	54 18 04	6.4	2.5	1.25 \pm 0.23	0.45 \pm 0.14	H9	XB; Note
P 7	14 2 27.9	54 12 50	6.8	2.9	0.35 \pm 0.13	0.09 \pm 0.15	H11	star
P 8	14 2 28.2	54 16 29	12.1	7.3	1.01 \pm 0.06	0.43 \pm 0.08	H10,TFR2	PHv; NGC5447: XB+DX; Note
P 9	14 2 29.9	54 21 21	11.9	7.0	0.33 \pm 0.07	-0.17 \pm 0.08	H13	star
P10	14 2 47.0	54 27 00	3.6	1.1	0.97 \pm 0.40	0.33 \pm 0.25	H17	galaxy
P11	14 2 52.9	54 21 15	5.5	1.8	1.23 \pm 0.32	0.32 \pm 0.18	H18	AGN
P12	14 3 00.8	54 14 28	4.5	1.3	1.73 \pm 0.87	-0.23 \pm 0.24		NGC5455: DX
P13	14 3 03.9	54 27 36	11.1	6.1	0.96 \pm 0.07	0.28 \pm 0.09	H19,TFR5	XB, SNR MF37
P14	14 3 05.2	54 07 25	4.5	1.7	0.66 \pm 0.26	0.15 \pm 0.20	H21	
P15	14 3 06.0	54 03 59	6.9	3.8	0.12 \pm 0.12	-0.32 \pm 0.14	H20	PHv; star
P16	14 3 12.6	54 21 04	5.9	2.0	-0.07 \pm 0.12	0.14 \pm 0.17	H23	nucleus of M101+DX
P17	14 3 15.2	54 17 56	4.2	1.3	-0.10 \pm 0.20	0.17 \pm 0.28	H22+H25	DX; Note
P18	14 3 19.6	54 17 20	7.4	3.0	0.72 \pm 0.13	0.30 \pm 0.12	H28	PHv; XB or AGN
P19	14 3 22.2	54 19 52	8.1	3.5	0.58 \pm 0.13	0.74 \pm 0.11	H29+30	SNRs
P20	14 3 28.5	54 21 24	3.8	1.1	0.07 \pm 0.20	-0.47 \pm 0.22		DX; Note
P21	14 3 36.0	54 19 30	4.7	1.5	0.49 \pm 0.27	0.79 \pm 0.22	H36	SNR; Note
P22	14 3 40.7	54 19 02	6.4	2.4	0.78 \pm 0.20	0.04 \pm 0.16	H37	NGC5461; DX
P23	14 3 41.8	54 31 40	5.2	2.0	0.53 \pm 0.19	-0.21 \pm 0.18		star: $B = 20.7, R = 18.8$
P24	14 3 49.7	54 24 14	3.9	1.2	0.90 \pm 0.39	0.39 \pm 0.24	H38	AGN
P25	14 3 53.7	54 21 57	8.0	3.3	0.53 \pm 0.13	0.23 \pm 0.13	H39+H40+H41	NGC5462
P26	14 4 00.1	54 09 00	6.3	2.8	0.48 \pm 0.16	0.47 \pm 0.15	H43	AGN
P27	14 4 00.1	54 11 40	5.0	1.8	1.06 \pm 0.33	0.09 \pm 0.21	H44,TFR7	AGN
P28	14 4 14.0	54 26 06	18.6	16.7	0.88 \pm 0.04	0.18 \pm 0.05	H45,TFR8	PHv; XB; Note
P29	14 4 15.4	54 09 58	6.0	2.6	0.53 \pm 0.18	0.21 \pm 0.18	H46	AGN or star
P30	14 4 16.2	54 16 16	6.7	2.8	0.66 \pm 0.16	0.27 \pm 0.14	H47	
P31	14 4 21.8	54 19 18	8.5	4.2	0.37 \pm 0.10	-0.17 \pm 0.11	H48	star
P32	14 4 28.9	54 23 48	6.8	3.0	0.52 \pm 0.14	-0.29 \pm 0.13	H49	SNR NGC5471B
P33	14 4 55.8	54 23 54	5.3	2.4	1.27 \pm 0.49	-0.28 \pm 0.21	H51	galaxy

^a Count rates are in the PSPC hard band. The definition of the hardness ratios are given in the text. XB - X-ray Binary in M101; DX - diffuse X-ray emission region in M101. See also Notes to Tables 3 and 4. Additional notes to individual sources:

- P6: A strongly variable, point-like RHRI source, which is apparently embedded in a well-developed outer spiral arm and is close to an H II region. The hard spectral characteristics suggests that the source is dominated by an X-ray binary.
- P8: Resolved by the RHRI into a bright point-like source plus an apparently diffuse feature associated with GHC NGC5447. This whole X-ray-emitting complex is within a spiral arm. The hard spectral characteristics indicates that the complex is located within or behind a dense cloud.
- P17: The 0.5-2 keV band emission may account for both H22 and H25, which are all marginally resolved by the RHRI (Fig. 12). The 1/4 keV band emission peaks in the region enclosed by various H II nebulae and by X-ray sources H22, H25, and H28. This apparently diffuse soft emission explains the low HR1 value of the PSPC source.
- P21: The RHRI counterpart H36 may represent the SNR MF83, one of the largest SNRs in M101. The PSPC aperture may also include a significant diffuse soft X-ray contribution.
- P28: Strongly variable by a factor $\gtrsim 2$ on time scales of days and in the direction of a spiral arm, but apparently not associated with a GHC.

Table 6: X-ray Spectral Properties of M101^a

Model Parameter	Value ^b
Thermal Plasma + Thermal Plasma	
T_{low} (keV)	0.186(0.179-193)
T_{high} (keV)	17(≥ 5.1)
N_H (10^{19} cm $^{-2}$)	2.6(1.5-3.8)
$\chi^2/n.d.f.$	51.6/50
Thermal Plasma + Power Law	
T (keV)	0.187(0.180-0.193)
Photon Index	1.37(1.13-1.55)
N_H (10^{19} cm $^{-2}$)	2.8(1.5-4.1)
$\chi^2/n.d.f.$	51.6/50

^a Metal abundances for both X-ray-emitting and -absorbing materials are assumed as 100% solar.

^b 90% confidence intervals (or limits) are included.

TABLE 7
PARAMETERS OF SELECTED GALAXIES

Galaxy	d (Mpc) ^f	Type ^a	D_{25} ^a (kpc)	i ^a ($^{\circ}$)	N_H ^b	$\log M_{HI}$ ^c (M_{\odot})	$\log L_B$ ^d (ergs s $^{-1}$)	$\log L_{FIR}$ ^e (ergs s $^{-1}$)	L_x ^f	N_{SLS} ^g
M33	0.72	Scd	12	57	6.0	9.1	43.20	42.23	0.08	0
M31	0.63	Sb	36	78	6.0	9.6	44.04	42.38	0.29	0
NGC253	2.6	Sc	19	86	1.3	9.8	43.65	43.50	0.78	1
M101	7.2	Sc	14	17	1.1	10	43.95	43.54	1.3	5
M51	7.7	Sc	24	20	1.3	9.5	44.07	43.68	2.9	7
M100	17	Sbc	35	27	2.3	9.7	44.42	43.74	5.5	6
M83	8.9	Sc	29	24	4.0	10	44.17	44.17	3.6	7

^a Tully (1988)

^b Galactic foreground absorption in units of 10^{20} cm $^{-2}$ (Dickey & Lockman 1990)

^c Neutral hydrogen mass (Tully 1988)

^d Blue luminosities (Tully 1988)

^e Far infrared luminosities, calculated from the IRAS 60 μ m and 100 μ m fluxes, using the expression $L_{FIR} = 3.65 \times 10^5 (2.58 S_{60\mu m} + S_{100\mu m}) d^2 L_{\odot}$ (cf. Devereux & Eales 1989). IRAS fluxes are from Soifer et al. (1989) and Rice et al. (1988).

^f Total 0.1-2.4 keV band X-ray luminosities (in units of 10^{40} ergs s $^{-1}$): M33 (Schulman & Bregman 1995; Long et al. 1996), M31 (Supper et al. 1987), NGC253 (Read, Ponman & Strickland 1997), M101 (this work), M51 (Ehle, Pietsch & Beck 1995), M100 (Immler, Pietsch & Aschenbach 1998), and M83 (Ehle et al. 1998).

^g Approximate number of superluminous sources associated with the galaxies.